

# Laser diffraction by periodic dynamic patterns in anisotropic fluids

Thomas John<sup>1,2</sup>, Ulrich Behn<sup>2</sup>, and Ralf Stannarius<sup>1,3</sup>

<sup>1</sup> Institut für Experimentelle Physik I, Universität Leipzig, Linnéstrasse 5,

<sup>2</sup> Institut für Theoretische Physik, Universität Leipzig, Vor dem Hospitaltore 1, D-04103 Leipzig, Germany

<sup>3</sup> Institut für Experimentelle Physik, Universität Magdeburg, Universitätsplatz 2, D-39106 Magdeburg

Received: date / Revised version: date

**Abstract.** This paper describes the application of a laser diffraction technique to the study of electroconvection in nematic liquid crystal cells. It allows a real-time quantitative access to pattern wave lengths and amplitudes. The diffraction profile of the spatial periodic pattern is calculated and compared quantitatively to experimental intensity profiles. For small director tilt amplitudes  $\varphi$ , the phase grating generated in normally incident undeflected light and the first order term correction from light deflection is derived analytically. It yields an  $I \propto \varphi^4$  dependence of the diffracted intensity  $I$  on the amplitude of director deflections. For larger director tilt amplitudes, phase and amplitude modulations of deflection of light in the inhomogeneous director field are calculated numerically. We apply the calculations to the determination of the director deflection and measure growth and decay rates of the dissipative patterns under periodic excitation. Real time analysis of pattern amplitudes under stochastic excitation is demonstrated.

**PACS.** 4 2.70.Df (Liquid Crystals),  
 47.20.-k (Hydrodynamic instability),  
 78.20.-e (Optical Properties of bulk materials and thin films).

## 1 Introduction

Electrohydrodynamic convection (EHC) in nematic liquid crystals is one of the standard systems of dissipative pattern formation. It has been studied extensively during past decades. As a consequence of anisotropic properties of nematic phase, the system is particularly rich in morphology. Among the advantages of this system for experimental characterization are the easy control of electric excitation fields, convenient time scales and the straightforward observation techniques.

The equations describing the fundamental mechanism yield two dynamic regimes: conduction and dielectric structures. In addition to the primary instability toward simple roll patterns with wave vectors normal or inclined to the preferential alignment of the director (optic axis) of the system, a variety of secondary instabilities have been described. Besides the investigation of arrays of parallel rolls, scientific interest recently focussed on defect structures and localized convection states [1, 2, 3, 4, 5]. The most successful and widely used method for the investigation of the complex convection patterns is optical microscopy, based on the shadowgraph method [6]. It utilizes the deflection of light rays in the spatially modulated director field of the nematic. It has been applied to the determination of wave vectors, onset thresholds and subcritical fluctuations of convection. One of the problems encountered

in this very efficient observation technique is the complexity of the optics in the periodically deformed director field. Simulations of the optical profiles have been presented by several authors [6, 7, 8, 9, 10, 11, 12], and the consequences of in-plane director twist have been considered [13, 14]. Although light propagation in such a two-dimensionally inhomogeneous medium has been treated theoretically with different approximation methods, and the qualitative relation between director structure and observed intensity profile in the microscope is well established, the method fails to provide quantitative access to deflection amplitudes of the director field. With varying amplitudes of the spatially periodic director modulations, both the positions of focal planes of the patterns and the intensity profiles at given focal planes of the microscope change in a complex way. Thus, the power of the method lies primarily in a quantitative determination of the pattern wavelengths and the topology of defect structures. Moreover, a fast (real-time) observation of the pattern amplitude dynamics requires considerable bandwidth and signal processing speed.

The wave vector spectrum can be determined qualitatively from a Fourier transform of digitized microscopic transmission images [12, 15, 16]. A more efficient, quantitative way is the quasi-optical Fourier transformation by means of laser diffraction. Laser diffraction has been applied earlier to the study of Williams domains or com-

parable dissipative patterns of nematics by Akahoshi et al. [17], Vistin and Yakovenko [18] and Miike et al. [19]. In these studies, the evaluation of the scattering profile remained to a large extent qualitative. A first experimental and theoretical study of the laser diffraction efficiency of EHC has been presented by Carroll [20], and Kashnow [21]. Scattering spots designated to gratings in phase and amplitude of transmitted light can be distinguished. They are generated by spatially modulated optical path and light deflections, respectively.

In a structurally similar system, Bouvier and Scharf have employed the Jones matrix method to calculate the diffraction efficiency of periodically deformed director fields in cells with structured electrodes and compared it to experimental data [22]. Their method depends upon the assumption of normal undeflected light transmission through the medium and describes only the phase grating.

Comprehensive analysis of diffraction gratings formed by EHC has been presented by Zenginoglou, Kosmopoulos and Papadopoulos [9, 23, 24, 25, 26]. Various aspects of laser diffraction by EHC have been considered, like the test of the validity of geometrical optics [25], diffraction under oblique incidence [23], director oscillations and relaxation, and the dielectric regime [26, 27]. In a study of stochastically excited EHC [28, 29, 30], laser diffraction has been successfully applied to characterize fundamental scaling laws in the statistical description of pattern dynamics. The advantage of the laser diffraction technique over shadowgraph observations is particularly evident in such an experiment where data reduction is necessary to process pattern wavelengths and the trajectory of the pattern amplitude in real time.

The previous study of fundamental scaling laws in stochastically driven EHC was based on several properties of the diffraction profiles which have not been explicitly given there [28, 30]. This manuscript deals with the underlying optical principles, it provides a justification of the quantitative relations between diffraction profiles and director field deflection amplitudes, and moreover, derives the absolute diffraction efficiencies which allow the determination of not only growth rates and relative pattern amplitudes but also the director tilt amplitudes in a quantitative way. We demonstrate the application of the laser diffraction technique to the study of amplitude dynamics of deterministically and stochastically excited patterns. A rigorous treatment of light propagation in two-dimensionally inhomogeneous director fields of EHC has not been presented so far, therefore we will discuss the validity of several approximations. We recollect the methods to calculate light propagation and the corresponding phase and amplitude modulations in two-dimensionally inhomogeneous director fields. A weakly nonlinear analytical calculation is compared with numerical simulations of the full nonlinear equations and with quantitative experimental data.

The paper is organized as follows: a short introduction into the basic principles of the Carr-Helfrich mechanism and the involved dynamic equations is given in the second section. We introduce the experimental setup and the qualitative structure of the diffraction patterns in the

third section. In Sec. 4, we derive the analytical formula for the phase and amplitude gratings generated by a weakly distorted director field, which also accounts for first order effects of light deflection. In the course of the fourth section, the quantitative numerical calculation of the diffraction profile is performed. Although a great part of the equations derived in this section have been communicated in earlier work by other authors, we consider it helpful to include a comprehensive treatment of the optical background here, in particular because in literature sometimes there seem to be contradictory details of the calculations (see below). One obtains numerically the phase and amplitude gratings produced by the mesogen layer for normal and oblique incidence of monochromatic light. This allows quantitative predictions from the combined effects of ray deflection and optical path length modulation. We describe the diffraction efficiency of periodic nematic director structures and compare our calculations with the approaches proposed in literature. The numerical and analytical results are tested by comparison with the experiment. Finally, we apply the method to the determination of growth rates and Lyapunov exponents of pattern amplitudes in EHC and demonstrate the power of the method to determine real-time amplitude fluctuations of director field modes.

## 2 Electroconvection

Electrically driven convection in liquid crystals bases on the interaction of free charges in the mesogen with external electric fields, and the coupling of fluid flow to the deflection of the nematic director. A comprehensive review is given, e.g., in Refs. [31, 32, 33, 34]. The essential variables describing the structures are the spatially modulated charge distribution  $\tilde{q}(x, y, z)$  and the director tilt angle  $\tilde{\varphi}(x, y, z)$ , both are coupled via the electrohydrodynamic equations. In an oscillating excitation field, the two quantities have qualitatively different dynamic behaviour. For the diffraction experiment as well as for the conventional shadowgraph images, only the director field modulation is relevant and accessible.

A sketch of the experimental geometry is given in Fig. 1. The nematic director alignment at the glass plates is fixed along  $x$  by surface treatment. The ground state is a uniform director field in the cell. When an electrical field  $E = U/d$  is applied between the transparent ITO-electrodes at the glass plates, free charge carriers (ionic impurities or dopants) in the nematic fluid are accelerated and initiate a macroscopic flow. The conductivity anisotropy of the material in combination with small fluctuation modes of the director tilt lead to lateral charge separation in  $x$  direction and a periodically modulated flow field, which in turn couples to the director field by hydrodynamic equations. At the critical field  $E_c$ , stabilizing elastic and dielectric torques on the director are outmatched by destabilizing hydrodynamic torques. Under standard conditions, the system exhibits a forward bifurcation to normal rolls (wave vector along the easy axis of the director) or to oblique

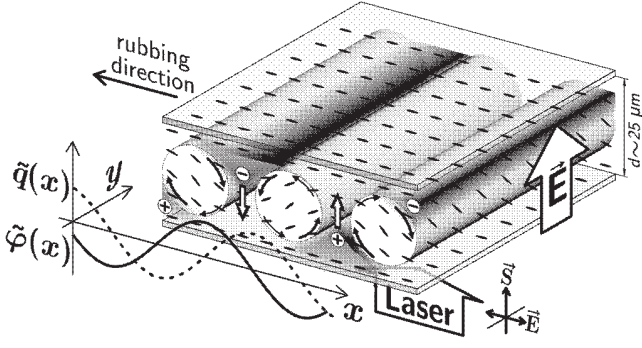


**Fig. 1.** Schematic drawing of convection rolls and director field in a nematic sandwich cell. A snapshot of the spatial modulations of director and charge fields ( $\tilde{\varphi}, \tilde{q}$ ) in the cell midplane is sketched.

rolls. Threshold voltage and critical wave number are frequency dependent. The pattern stability diagram of the two sandwich cells studied here is shown in Fig. 2. The nematic material is *Mischung 5*, a mixture of four di-substituted phenyl-benzoates [28], material parameters in Table I. The first cell has been prepared with the pure, undoped material, which has a low conductivity and correspondingly low cut-off.

The nematic mixture in sample 2 has been doped with 0.5 mass% tetrabutyl-ammonium bromide. Therefore its conductivities are much higher and the increased amount of charge carriers shifts the cut-off frequency out of the frequency range of measurements. It leads to a much more stable pattern amplitude characteristics near the threshold. In the undoped material, the content of charge carriers is comparably small ('natural' impurities after synthesis) and in the experiment, the threshold voltage is subject to certain small but measurable long-term fluctuations.

In Fig. 2, one distinguishes the low frequency 'conduction' regime and the high frequency 'dielectric' regime of cell 1, with a distinct jump in the wave number at the cut off frequency. Only the low frequency regime is in the accessible frequency range in cell 2. All measurements in this study are performed in the conduction regime, where the director field performs only moderate oscillations synchronous with the excitation frequency, but keeps its sign during the field cycles. However, there is no principal limitation for an application of the presented setup to structures of the dielectric regime [26, 27, 35].

The mathematical description is based on the Maxwell and Navier Stokes equations. The linear stability analysis of the torque balance uses a test mode ansatz for director deflections and charge density modulations

$$\tilde{\varphi}(x, z, t) = \varphi_t \cos(k_x x) \cos(k_z z), \quad (1)$$

$$\tilde{q}(x, z, t) = q_t \sin(k_x x) \cos(k_z z), \quad (2)$$

where  $k_x$  is the periodicity of the pattern. Because the director is fixed parallel at the glass plates, the boundary conditions  $\varphi(\pm z = d/2) = 0$  enforce  $k_z = (2n + 1)\pi/d$ ,  $n$  integer. Near onset, we consider only the ground mode  $k_z = \pi/d$ . In the investigated parameter regions here only

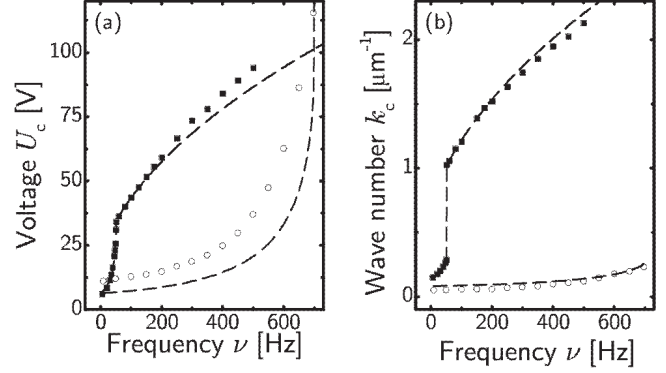


**Fig. 2.** Stability diagram of the electroconvection patterns at the first instability measured for cell 1 (25.8  $\mu\text{m}$  thick,  $\blacksquare$ ) and cell 2 (48.5  $\mu\text{m}$  thick,  $\circ$ ) under square wave excitation. The thresholds under sine wave excitation are not much different from the square wave case (at comparable effective voltages). Lines are from the analytical calculation, where known material parameter from independent experiments, have been used, if available. The remaining unknown parameter have been obtained from the fit to the experimental data. The cut off frequency  $\nu_c = 51$  Hz for cell 1 separates conduction and dielectric regimes. In case of cell 2 the much higher cut-off frequency is outside of the presented range.

normal rolls appear, and no  $y$  dependence has to be considered. Linearization leads to a linear ordinary differential equation system in  $(q, \varphi)$ . The solution for a constant electric field amplitude  $E$  involves a  $2 \times 2$  non-symmetric time evolution matrix  $\mathbf{T}$  [36] which depends on the wave vector  $k_x$  of the particular test mode

$$\begin{pmatrix} q \\ \varphi \end{pmatrix}(t) = \mathbf{T}(E, k_x, t) \begin{pmatrix} q \\ \varphi \end{pmatrix}(0). \quad (3)$$

At square wave excitation, where only the sign of  $E$  alternates, the time evolution at points with alternating sign of  $E$  is given by a product of matrices with constant coefficients

$$\begin{pmatrix} q \\ \varphi \end{pmatrix}(t_n) = \mathbf{T}^\pm(\Delta t_n) \cdots \mathbf{T}^\mp(\Delta t_1) \mathbf{T}^+(\Delta t_0) \begin{pmatrix} q \\ \varphi \end{pmatrix}(0), \quad (4)$$

$$t_n = \sum_{i=0}^n \Delta t_i, \quad E(t) = \pm E, \quad (5)$$

where  $\Delta t_i$  are the time intervals between consecutive jumps. The solution at intermediate times is calculated with Eq. (3). The involved material parameters are listed in Table 1, further details are given in [36].

The largest of the two real eigenvalues of the matrix product in Eq. (4) is related to the Lyapunov exponent of the system [36] and describes the asymptotic behaviour of a small initial perturbation in  $(q, \varphi)$ . In case of a periodic excitation, all  $\Delta t_i = \Delta t = 1/(2\nu)$  are equal and after  $n$  full periods of the ac excitation, the product in Eq. (4) can be split in repeated blocks of the product  $\mathbf{T}^+ \mathbf{T}^-$

$$\begin{pmatrix} q \\ \varphi \end{pmatrix}(t_n) = (\mathbf{T}^+ \mathbf{T}^-)^{n/2} \begin{pmatrix} q \\ \varphi \end{pmatrix}(0). \quad (6)$$

For  $t_n \gg \Delta t$ , the amplitudes of both variables grow or decay exponentially, and the (dimensionless) largest real eigenvalue  $\lambda_1(E, k_x, \nu)$  of  $\mathbf{T}^+ \mathbf{T}^-$  gives the growth or decay rate  $\nu \lambda_1$ . The maximum  $\lambda_1(E, k_x, \nu)$  of all  $k_x$  selects the critical wave number  $k_c$ . The theoretical threshold field  $E_c$  at a given frequency  $\nu$  is determined by the first positive value of  $\lambda_1(E, k_c, \nu)$  with increasing  $E$ . This value coincides with results from the Floquet theorem.

With any optical detection methods (shadow graph or diffraction), only  $\varphi_t$  is observable and asymptotically for  $t \gg \Delta t$ , (in the limit of small  $\varphi_t$ )

$$\varphi_t = \varphi_0 e^{\nu \lambda_1 t}, \quad (7)$$

where,  $\varphi_0$  is the initial amplitude of the considered mode, related to fluctuations of director and charge fields. For large amplitudes,  $\varphi_t$  is limited by nonlinearities that will not be considered in the linear treatment. For sample 1, the theoretical threshold curves  $U_c(\nu) = E_c d$  and  $k_c(\nu)$  can be fitted to the experimental data over a wide frequency range with most of the involved material parameters taken from independent experiments, see Table I. Some remaining unknown viscoelastic parameters are obtained from the fit. With this completed set of parameters, the theoretical  $\lambda_1(E, k_c, \nu)$  dependence can be calculated analytically as a function of the excitation frequency  $\nu$ .

### 3 Laser diffraction experiment

The diffraction of laser light by the director pattern provides the opportunity to analyse the spatial mode spectrum in real time. Figure 3 sketches the experimental setup consisting of a low power ( $\approx 1$  mW) He-Ne laser, the liquid crystal (LC) cell mounted in a Linkam microscope hot stage TMS 600, a photodiode or alternatively a diffusely reflecting screen for 2D camera images.

The photodiode can be moved by a stepper motor in horizontal  $x$  direction across the scattering image. Its aperture is  $3 \text{ mm} \times 3 \text{ mm}$ . At a distance  $\ell$  of approx 800 mm from the LC cell, this corresponds to an angular resolution of 5 mrad. The 2D images of the CCD camera are used for the qualitative characterization of the diffraction patterns only (see appendix), while all quantitative intensity measurements are performed with the photodiode.

The test modes of Eqs. (1,2) correspond to a one-dimensional stripe pattern along  $x$  in the microscope image. For the sample cell 1 studied here, it appears at intermediate frequencies, from the Lifshitz-point (below 20 Hz) to the cut-off frequency ( $\approx 50$  Hz), as the first instability. At lower frequencies, the wave vector at onset has a non-zero  $y$  component.

Figure 4 demonstrates the two cases of normal and oblique rolls for square wave excitation at 30 Hz and 10 Hz, resp., at voltages slightly above the convection threshold. In such cases where one or two superimposed wave vectors form the spatial structure, the diffraction experiment provides the pattern wave lengths, orientations and amplitudes. Defects and domain sizes will primarily influence width and fine structure of individual diffraction peaks but are not directly accessible from the profiles.

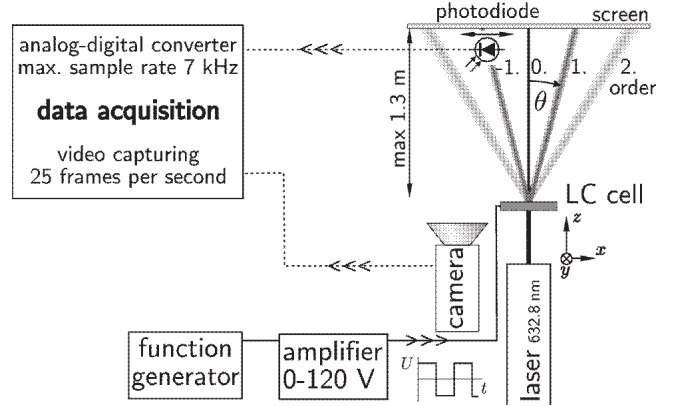


**Fig. 3.** Sketch of the experimental setup. The driving voltages are synthesized by a computer with digital analog (DA) converter and analog amplifier. The photodiode signal is sampled by the computer at a maximum rate of 7 kHz with an accuracy of 12 bit, or alternatively sampled by a digital voltmeter at a rate of 50 Hz with an accuracy of at least 6 digits.

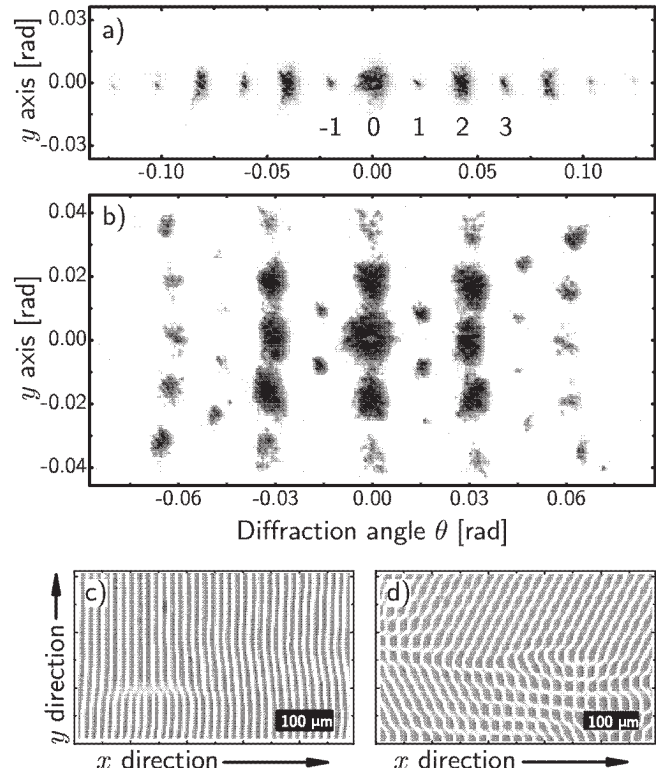


**Fig. 4.** Snapshots of diffraction images (a,b) and respective microscope images (c,d) for normal rolls at 30 Hz (a,c) and oblique rolls at 10 Hz (b,d), cell 1. Numbers in (a) mark the diffraction order. In the lower left part in (c), a localized defect of the roll pattern is visible. The cell thickness is  $25.8 \mu\text{m}$ .

## 4 Optics

### 4.1 Light propagation

The light intensity at the position of the diffraction reflexes is directly related to the amplitude of the spatial director mode. The problem of light propagation in a periodically modulated director field has been investigated by different groups before [8,9,20,21,22]. These previous works can be grouped into two different approaches. One is based on the solution of the Maxwell equations, the calculation of the spatial distribution of  $\mathbf{E}$  and  $\mathbf{D}$ . Yet, a complete solution of the Maxwell equation with boundary conditions can only be obtained numerically for the present problem. A linearized wave propagation approach can be found, for example, in Ref. [25]. The alternative method is based on the calculation of light ray's using the eikonal method [37] or crystal optical methods [9,24]. Here, we give a short outline of the calculation of phase and amplitude of the laser light passing the LC layer using crystal optics.

The polarization vector  $\mathbf{E}$  of the incident laser light is adjusted along the director easy axis, since only the extraordinary wave is relevant for the diffraction effect (see Fig. 1). Ordinary rays pass the LC layer without deflections and phase modulation.

In the lowest order of approximation, we may assume a straight propagation of the electromagnetic wave without any deflection of the light beam,  $r(z; x_0)$  being the  $x$ -coordinate of the ray

$$r'(z; x_0) = dr(z; x_0)/dz = 0 \quad (8)$$

$$r(z; x_0) = x_0. \quad (9)$$

It yields no amplitude modulation but a first estimation of the phase profile of the light that has penetrated the cell. Under these assumption the phase  $\psi_s(x)$  in dependence on the amplitude of director deflections is given by (see Fig. 5)

$$\psi_s(x) = k_L \int_{-d/2}^{d/2} n_{\text{eff}}^p(r, r', z) dz = k_L n_e d + \Delta\psi_s(x), \quad (10)$$

$$n_{\text{eff}}^p(\tilde{\beta}) = \frac{n_o n_e}{\sqrt{n_o^2 \cos^2 \tilde{\beta} + n_e^2 \sin^2 \tilde{\beta}}}, \quad (11)$$

$$\tilde{\beta}(r, r', z) = \varphi_t \cos(k_x r) \cos(k_z z), \quad (12)$$

$$\Delta\psi_s(x_0) \approx -k_L n_e d \frac{n_e^2 - n_o^2}{8n_o^2} \varphi_t^2 \cos(2k_x x_0), \quad (13)$$

where  $n_{\text{eff}}^p$  is the effective refractive index and  $n_o, n_e$  are the ordinary and the extraordinary refractive indices of the nematic material (see Table 1). Only the first non constant term in the series expansion of  $n_{\text{eff}}^p$  enters the result, the constant phase does not contribute to the diffraction profile.

The exact calculation of light propagation basing on the calculation of ray paths ( $r(z; x_0), z$ ) uses the FERMAT principle. From the symmetry of the problem, no change

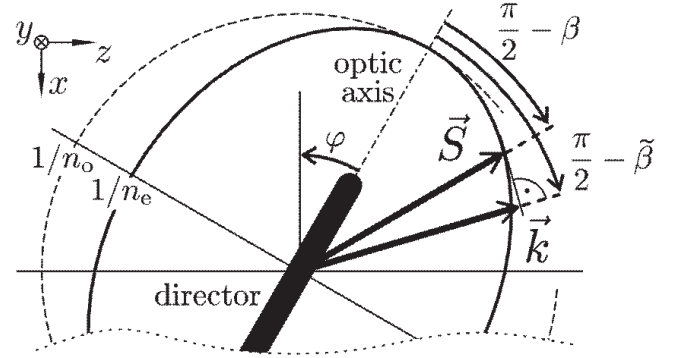


**Fig. 5.** Definition of angles on the ray ellipsoid,  $\varphi$  : director deflection,  $\pi/2 - \beta$  : angle between optic axis and Poynting-vector  $\mathbf{S}$ ,  $\pi/2 - \tilde{\beta}$  : angle between optic axis and normal of plane wavefront  $\mathbf{k}$ .

of polarization of the light can occur. If the wave number of the laser light  $k_L$  is much larger than the wave number of the pattern, the FERMAT principle can be applied in the birefringent material. The minimum condition is

$$\int_{-d/2}^{d/2} n_{\text{eff}}^r(r, r', z) dz = \min, \quad (14)$$

$$n_{\text{eff}}^r(r, r', z) = \sqrt{n_e^2 \cos^2 \beta + n_o^2 \sin^2 \beta}, \quad (15)$$

$$\beta(r, r', z) = \varphi_t \cos(k_x r) \cos(k_z z) - \arctan r', \quad (16)$$

$$ds = \sqrt{1 + r'^2} dz, \quad (17)$$

where  $n_{\text{eff}}^r$  is the effective ray index<sup>1</sup>. Applying the EULER-LAGRANGE formalism leads to a ordinary differential equation of second order in the displacement  $r(z; x_0)$  of a ray

$$r'' = \varphi_t \frac{n_e^2 - n_o^2}{n_e^2 n_o^2} (1 + r') (t_1 + t_2), \quad (18)$$

$$t_1 = k_z \cos(k_x r) \sin(k_z z) (n_e^2 \cos^4 \beta - n_e^2 r' \cos^3 \beta \sin \beta - n_o^2 r' \cos \beta \sin^3 \beta - n_o^2 \sin^4 \beta),$$

$$t_2 = k_x \sin(k_x r) \cos(k_z z) (n_e^2 r' \cos^4 \beta + n_e^2 \cos^3 \beta \sin \beta + n_o^2 \cos \beta \sin^3 \beta - n_o^2 r' \sin^4 \beta).$$

Eq. (18) is an exact result which we use in a RUNGE-KUTTA algorithm for a numerical computation of the ray paths. Expanding of (14) to first order in the amplitude  $\varphi_t$  of the spatial mode of director deflection yields

$$r'' \approx \frac{n_e^2 - n_o^2}{n_o^2} \varphi_t k_z \cos(k_x r) \sin(k_z z). \quad (19)$$

The integration of Eq. (19) with the initial values

$$r|_{z=-d/2} = x_0, \quad r'|_{z=-d/2} = 0 \quad (20)$$

<sup>1</sup> In literature, e.g. [6,38,39], there has sometimes been a confusion about the appropriate usage of the ray index or refractive index in the computation of light propagation through a birefringent nematic layer with periodically deformed director field.



and the approximation  $\cos(k_x r) = \cos(k_x x_0)$  leads to a path which enters at  $x_0$  and

$$r(z; x_0) = x_0 - \frac{1}{k_z} \frac{n_e^2 - n_o^2}{n_o^2} \varphi_t (1 + \sin k_z z) \cos k_x x_0. \quad (21)$$

To describe the focussing effect in the shadowgraph method the second order term in  $\varphi_t$  must be considered, it can be found in Ref. [6]. For the diffraction pattern, mainly the phase is important (at least for small director deflections) and therefore no consideration of higher order terms are necessary. In order to calculate the resulting phase beyond the cell, we have to distinguish between the direction of propagation of energy flux  $\mathbf{S}$  and the normal of wavefronts  $\mathbf{k}$  (Fig. 5). In uniaxial birefringent material the relation is [40]

$$\tan\left(\frac{\pi}{2} - \tilde{\beta}\right) = \frac{n_e^2}{n_o^2} \tan\left(\frac{\pi}{2} - \beta\right). \quad (22)$$

The phase can be calculated using different indices

$$\frac{\psi}{k_L} = \int n_{\text{eff}}^r ds = \int n_{\text{eff}}^p d|\mathbf{k}| = \int n_{\text{eff}}^p \cos(\beta - \tilde{\beta}) ds. \quad (23)$$

Finally, the calculated lateral phase difference along curved paths at the exit position for small director deflections is basically the same as the result for straight transmission (13)

$$\Delta\psi(r, z)|_{z=d/2} = \Delta\psi_s(x_0). \quad (24)$$

This result is in agreement with the relation in [37] calculated from the eikonal equation. Also, the next order term in  $\varphi_t^3$  is stated in [37]. The consideration of the displacement  $r(z; x_0) - x_0$  gives

$$\Delta\psi(\tilde{x}, z)|_{z=d/2} \approx -k_L n_e d \frac{n_e^2 - n_o^2}{8n_o^2} \varphi_t^2 \cos(2k_x \tilde{x}), \quad (25)$$

$$\tilde{x} = r(d/2; x_0), \quad (26)$$

$\tilde{x}$  denotes the exit position  $r(d/2; x_0)$  of a beam entering at  $x_0$  which may differ from  $x_0$  due to the ray deflection. Therefore, the first order bend of the light paths is an effect of the birefringence (the inclination of the optic axis of the nematic material respective to the incident beam direction) and is not the result of the periodic modulation of the refraction (connected with the ray index) in  $x$ -direction.

The displacement of the rays after propagating the cell and the conservation of energy gives the intensity  $\mathcal{I}$  in terms of the incident intensity  $\mathcal{I}_0$ , and the amplitude of the electric field  $\mathcal{E}$  (with  $\mathcal{E}^2 \propto \mathcal{I}$ ) in the exit plane

$$\mathcal{I}_0 \delta x_0 = \mathcal{I} \delta \tilde{x}, \quad (27)$$

$$\mathcal{I}_0 dx_0 = \mathcal{I} [r(z; x_0 + dx_0) - r(z; x_0)]|_{z=d/2}, \quad (28)$$

$$\frac{\mathcal{I}}{\mathcal{I}_0} = \frac{\mathcal{E}^2(\tilde{x})}{\mathcal{E}_0^2} = \left(1 + 2 \frac{k_x}{k_z} \frac{n_e^2 - n_o^2}{n_o^2} \varphi_t \sin k_x x\right)^{-1}. \quad (29)$$

The ansatz (19) is only correct in the limit of small  $\varphi_t$  when rays leaving the cell in parallel in good approximation. A correction resulting from more exact treatment based on  $\nabla \mathbf{S} = 0$  can be found in Ref. [9].

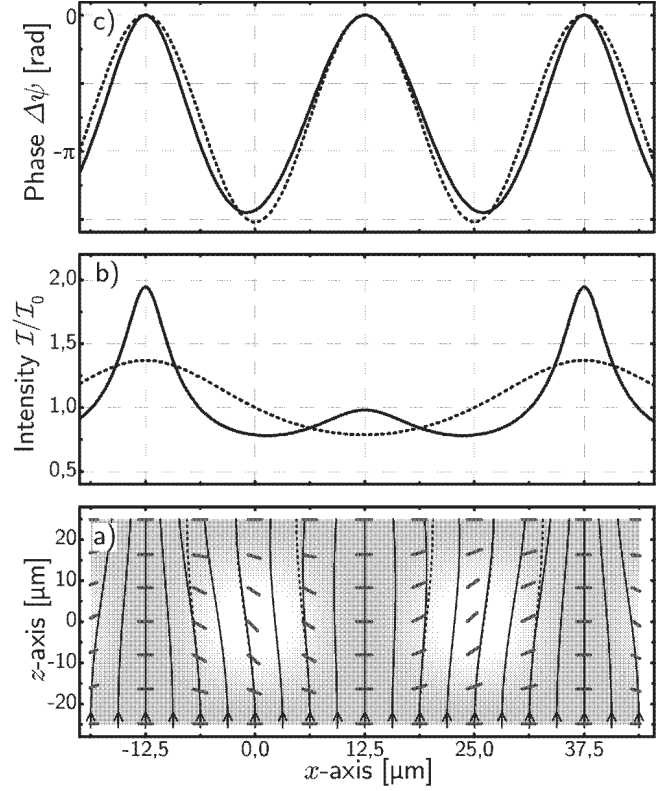


**Fig. 6.** Numerically (solid) and analytically (dotted) calculated ray propagation (a), intensity (b), and relative phase (c) of light after penetrating the nematic layer at  $z = 25 \mu\text{m}$ . The assumed director tilt ( $\varphi = 20^\circ$ ) is schematically depicted in (a), the grey scale visualizes the effective refractive index for straight light propagation. The periodicity of the amplitude grating is that of the director field. In contrast, the dominating phase modulation has twice the wave number of the director field. A cell thickness of  $50 \mu\text{m}$  and optical parameters of Tab. I have been assumed.

Figure 6a) illustrates the light propagation from different entry positions along the  $x$ -axis in the case of a strong director tilt amplitude  $\varphi = 20^\circ$ . It compares the numerically calculated paths with the analytical result from (21). Also the intensity and the phase at exit position are depicted in Fig 6b,c). The analytical result for the phase differs hardly from the exact numerical calculation whereas the first order approximation in intensity differs even qualitatively from the numerical values. Fortunately, the diffraction efficiency is dominated by the phase profile and therefore the conclusions drawn from diffraction profiles about director deflections are correct up to large deflections angles.

## 4.2 Diffraction profiles

The cell is illuminated with a normally incident planar wave, polarized in  $x$  direction. The area contributing to diffraction is a circular spot with radius  $s \approx 0.5 \text{ mm}$ . In general, the electric field at the rear of the cell can be

written as

$$\hat{\mathcal{E}}|_{z=d/2} = \mathcal{E}(x)e^{i\Delta\psi(x)}, \quad (30)$$

with the amplitude  $\mathcal{E}(x)$  and  $\Delta\psi(x)$  the lateral phase difference of the wave at the position  $(x, z = d/2)$ . For a one-dimensional modulation (Eqs. (1,2)), each location  $x$  can be considered as the origin of a spherical wave. The diffraction intensity at  $\ell \gg s$  into the angle  $\theta$  in the  $(x, z)$  plane is

$$dE(x, \mathbf{k}_L; \mathbf{l}) = \frac{\mathcal{E}(x)}{\ell} e^{i[-\mathbf{k}_L \mathbf{l} + \Delta\psi(x)]} dx dy, \quad (31)$$

$$\mathbf{k}_L \mathbf{l} = k_L \ell - x k_L \sin \theta, \quad (32)$$

where  $k_L$  is the wave number of the incident light, the vector  $\mathbf{l}$  connects the cell with the detector position and  $\ell$  the distance between cell and detector. Integration over a circular area with radius  $s$  of the illumination spot gives the amplitude of the complex wave with the corresponding intensity

$$E(\theta) \propto \int_{-s}^s \int_{-\sqrt{s^2-y^2}}^{\sqrt{s^2-y^2}} \mathcal{E}(x) e^{i[x k_L \sin \theta + \Delta\psi(x)]} dx dy, \quad (33)$$

$$I(\theta) \propto |E(\theta)|^2. \quad (34)$$

To calculate the complete diffraction function numerically, we consider both the spatial modulation of  $\mathcal{E}(x)$  (amplitude grating) as well as the phase modulation  $\Delta\psi(x)$  (phase grating). Basically, the first one is effective for shadow graph images. In contrast, when the director modulation is small, the latter plays the dominating role in the diffraction characteristics. Therefore, we will consider for analytical approximations the phase grating alone.

In case of small director deflections, the differences between exit position  $\tilde{x}$  and entry point  $x_0$  can be neglected and the periodicity of the phase grating can be written as

$$\Delta\psi(x) = \Delta\psi_{\max} \cos(2k_x x). \quad (35)$$

It is twice that of the director field and therefor diffraction reflexes from the the phase grating appear only at even order  $n$ . On the other hand the periodicity of the amplitude grating (29) is the same of the director field and it contributes also on odd order reflexes.

The integration of (33) gives the intensities  $I_n = I(\theta_n)$  of the  $n$ -th order diffraction spots. With the assumptions  $\mathcal{E}(x) = \text{const.}$  and (35) the intensities at angles  $\theta_n$  are described by Bessel functions  $J_{n/2}$  with the amplitude of the laser light phase modulation in the argument

$$\frac{I_n(\varphi_t)}{I_0} = \frac{|E(\theta_n)|^2}{|E(\theta_0)|^2} = J_{n/2}^2(\Delta\psi_{\max}) \approx \frac{\Delta\psi_{\max}^n}{2^n [(n/2)!]^2}, \quad (36)$$

where  $I_0$  is the intensity of the mean beam at the ground state. Using (24) and (13) gives the final quantitative relation between normalized diffraction intensity and director tilt amplitude at the dominating second order reflex

$$\frac{I_2(\varphi_t)}{I_0} = \frac{1}{4} \left[ k_L n_e d \frac{n_e^2 - n_o^2}{8n_o^2} \right]^2 \varphi_t^4, \text{ where } I_2 \ll I_0. \quad (37)$$

The numerically obtained diffraction efficiencies in the limit of small  $\varphi_t$  confirm the relation (37) including the prefactor. The analytical approximations are satisfactory up to  $\varphi \sim 30^\circ$  for thin cells.

The numerical calculation offers an easy way to consider effects from oblique illuminations, an important point to understand the sensitivity of the diffraction images to a non perfect sample orientation. A detailed discussion is found in the appendix.

### 4.3 Experimental test

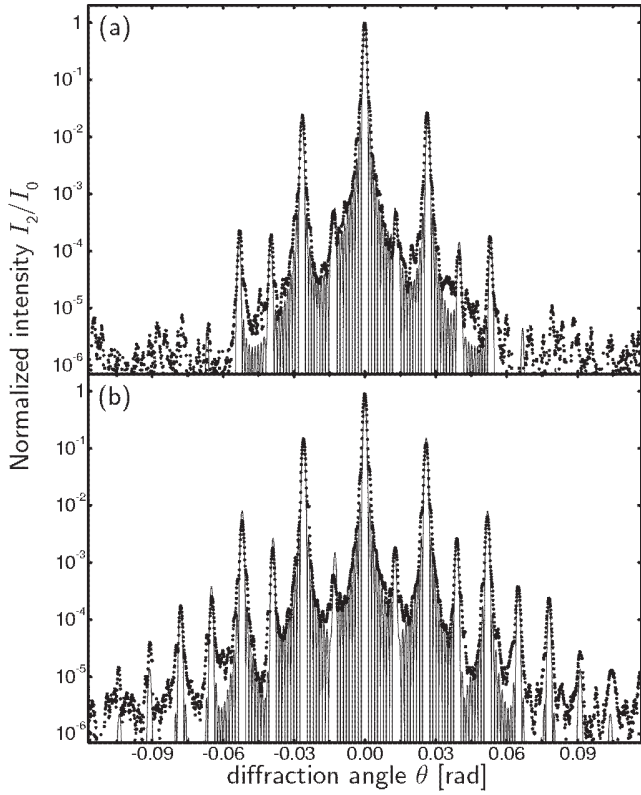
We tested the presented calculations with the setup sketched in Fig. 3 with sample 2. The temperature is stabilized at  $32^\circ\text{C}$  and the measurement is performed at 500 Hz sine excitation. Due the high conductivity the cut-off frequency is shifted above 600 Hz and the pattern is more permanent at 500 Hz sinodial excitation than in cell 1. A circular aperture with 0.5 mm in diameter defines the illumination spot. A smaller movable photo diode ( $0.3 \times 0.6$  mm) is positioned in a distance of  $\ell = 820$  mm, to obtain a high resolution in diffraction angle. The analog-digital-converter is a programmable Kethley multimeter with a resolution of 24 bit and a sampling rate of  $50\text{ s}^{-1}$ .

Figure 7 shows the baseline corrected intensity along  $x$  direction in the  $x$ - $z$  plane ( $y = 0$  in Fig. 4) for two applied voltages slightly above the instability threshold. All profiles are normalized with the transmitted primary beam intensity at  $\theta = 0$ . Note the logarithmic intensity scale. In order to discriminate the diffracted light from a small constant background (scattered light from glass plates and small amplifier offset), we subtract the constant signal of the order of  $10^{-4}$ , detected at large deflection angles ( $\theta > 0.5$  rad), from all measurements. In superposition with the constant offset, small fluctuations in order of  $10^{-7}$  are observed which drop below the detection level when the sample temperature is increased above  $80^\circ\text{C}$  into the isotropic phase. The intensity profiles are compared with numerical calculations for different director amplitudes. The best fits lead to director deflections  $\varphi = (7.4 \pm 0.3)^\circ$  and  $\varphi = (12.6 \pm 0.3)^\circ$ ,  $\epsilon = U/U_c - 1 \approx 2 \times 10^3$  and  $\epsilon \approx 5 \times 10^3$ , resp. (Fig. 7). The normalized intensity at the second order reflex coincides well with the value obtained from analytical treatment (Eq. (37)).

## 5 Applications

### 5.1 Study of EHC near the threshold

The sensitivity in the detection of small pattern amplitudes and the quantitative relation between diffraction intensity and director tilt provides the opportunity to study electroconvection near the onset threshold experimentally. Amplification of thermal fluctuations slightly below the threshold has been studied previously with the shadow-graph method [2, 4, 41, 42, 43].



**Fig. 7.** Comparison of numerical calculated diffraction profiles (solid line) and measured intensities (dots), normalized to the primary beam intensity. The measured profile at  $U = 28.79$  V (a) and  $U = 28.90$  V (b) corresponds to the calculation with amplitudes  $\varphi = 7.4^\circ$  (a) and  $\varphi = 12.6^\circ$  (b). The corresponding deflections from measured  $I_2/I_0$  using (37) are  $7.5^\circ$  and  $11.0^\circ$ . The pattern wave length  $\lambda_{\text{dir}} = 48 \mu\text{m}$ , cell thickness  $48.5 \mu\text{m}$ ,  $U_c = 28.73$  V.

For measurements near the instability threshold, we use cell 2. We study the stationary director deflection amplitude as a function of the control parameter  $\epsilon = U/U_c - 1$  by increasing the driving voltage gradually from a subcritical value to a voltage above the threshold. The voltage is increased adiabatically slowly such that the director deflection is always practically in equilibrium. Simultaneously, the diffraction intensity at the second order reflex is recorded as a quantitative measure of the director field modulation. The constant scattering background is eliminated as above. The experiment is repeated with the opposite direction of the field sweep, the diffraction intensity is recorded while the driving voltage is decreased with the same rate. The expected characteristics for a perfect forward pitchfork bifurcation is  $\varphi \propto \sqrt{\epsilon}$ . Considering relation (37), this would correspond to a quadratic dependence of the diffraction intensity at the second order reflex from the control parameter

$$I_2 \propto \varphi^4 \propto \epsilon^2. \quad (38)$$

Figure 8 shows the experimental results. For better visualization, data are presented in linear scale and logarithmic

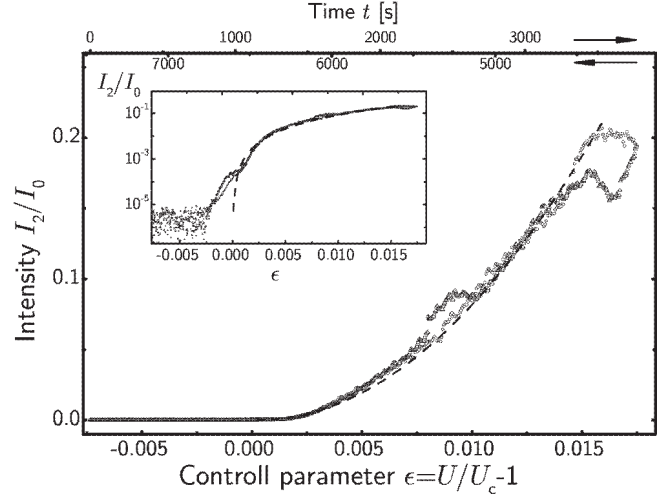


**Fig. 8.** Intensity at the second order peak within a sequence of increasing ( $\circ$ ) and decreasing ( $\triangle$ ) driving voltage in cell 2. The fit to a function  $I \propto (U - U_c)^2$  yields a critical voltage  $U_c = 28.84$  V at sine wave excitation with  $\nu = 500$  Hz. Due to a slow drift in conductivity the critical voltage is shifted to a higher value as in Fig. 7. In the insert, the same data are presented on logarithmic scale, an increase of fluctuation amplitudes in the subcritical voltage range is clearly observable.

mically in the insert. The systematic deviations of data taken during up and down sweeps of the field, resp., are negligibly small. No hysteresis is found. The parameter  $U_c$  is fitted such to obtain best agreement with Eq. (38). The measured intensities match the expected quadratic behaviour, and therefore we associate the fitted  $U_c$  with the threshold voltage. Close to the threshold and below  $U_c$ , the characteristics is covered by additional influences of noise. It clearly deviates from the prediction of Eq. (38) indicated by the dashed curve. One of the possible reasons is that subcritical fluctuations of the modes close to the instability threshold [2,4,41] lead to an increased diffraction signal at the corresponding position. In addition, the equations used in the hydrodynamic model use exact planar boundary conditions, while the cell actually has a small pretilt, typical for glass plates of sandwich cells with antiparallel rubbing.

## 5.2 Measurement of growth and decay rates at periodic excitation

The solution of the linearized differential equations (4) yield an exponential growth or decay of  $\varphi_t$  (7) in an electric field of constant amplitude. Equation (37) connects this amplitude of the director deflection with the measurable diffraction intensity, e.g. at the second order reflex. Both equations can be combined to

$$I_2(t) = I_2(0)e^{4\nu\lambda_1 t} = I_2(0)e^{\lambda_{\text{exp}} t}, \quad (39)$$

where  $\lambda_1(E, \nu, k_c)$  is the largest eigenvalue of the matrix product  $\mathbf{T}^+\mathbf{T}^-$  and  $\lambda_{\text{exp}}$  the experimentally determined



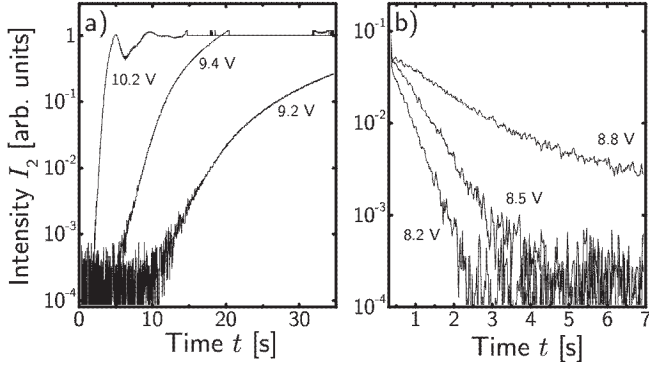


**Fig. 9.** Time evolution of the diffraction intensity at the second order reflex after changes of the field (20 Hz). The vertical axis shows the amplified voltage at the photo diode, which is proportional to the intensity  $I_2$ . The threshold  $U_c$  is 9 V in case of cell 1. In (a), the applied square wave voltage is switched at  $t = 0$  from zero to supercritical voltages. In (b), the excitation voltage is switched down to slightly subcritical values.

growth rate from the intensity change at the second order reflex. The factor 4 considers the fourth order dependence of the scattering intensity from the director deflection amplitude. Positive growth rates for  $\lambda_{\text{exp}} > 0$  can be obtained in the experiment by recording the intensity change at the reflex after an electrical field  $E > E_c$  is turned on. For the measurement of  $\lambda_{\text{exp}} < 0$ , the electric field is first switched to a supercritical value  $E > E_c$  where the convection pattern develops. Then, the field is suddenly changed to a value  $E < E_c$  and the intensity trace is recorded. Examples for these procedures in cell 1 are shown in Fig. 9. In order to detect the fast changes we use an analog-digital-converter with a lower resolution (12 bit) but much higher sampling frequency of 1 kHz. The constant background is eliminated and the data are fitted to exponential functions in the middle of the detection range. Growth and decay rates of 200 measurements are depicted in Fig. 10 together with the eigenvalue  $\lambda_1(E)$  calculated analytically from the material parameter in Table 1, and the factor 4 from Eq. (39), has been taken into account. There is good quantitative agreement with the linearized theory for electroconvection for driving voltages around the threshold.

### 5.3 Trajectories under stochastic excitation

If the deterministic voltage is replaced by a stochastic excitation sequence, the trajectory of the director deflection exhibits irregular changes in time. A statistical analysis of this phenomenon has been described in detail [28,29]. The measurement of the time dependent diffraction intensity provides a convenient tool to study the trajectories of pattern amplitudes in real time. Figure 11 shows the example of measured intensities at the second order reflex and the corresponding numerical simulation of the trajectory by solution of the differential equation (4).

The stochastic sequence in this experiment was a dichotomous Markov process (DMP) with jump rate  $160 \text{ s}^{-1}$ .

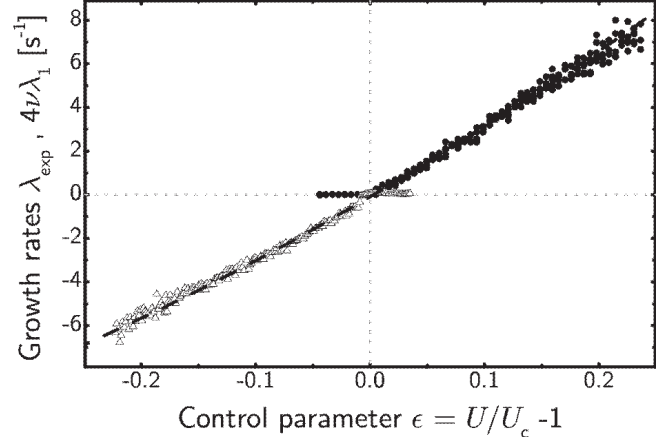


**Fig. 10.** Growth and decay rates at different excitation amplitudes (square wave). Growth rates ( $\bullet$ ) has been obtained from traces similar to those in Fig. 9a, and decay rates ( $\Delta$ ) from traces like those in Fig. 9b. The dashed line depicts the theoretical prediction  $4\nu\lambda_1(E)$  from a calculation of the largest eigenvalue of  $\mathbf{T}^+\mathbf{T}^-$  in Eq. (6). Material parameters are given in Table 1.

Since the excitation sequence is synthesized with a computer, it is possible to use identical noise sequences in both experiment and simulation. In the bottom part of Fig. 11, the realization of the stochastic driving process is shown. The numerical  $I(t)$  have been obtained from the  $\varphi(t)$  trajectories by use of (37). Figure 11 demonstrates that experiment and theory for stochastically excited EHC do not only agree on the statistical level when fundamental scaling laws are compared, but even in details of the trajectories to a satisfactory degree, when we take into account that the simulation cannot treat the involved additive noise exactly but substitutes it by some average [28]. Of course, even repeated measurements of experimental trajectories are not exactly reproducible because of such additive (thermal) noise. Trajectories taken with the same noise sequence of the driving field differ in detail at small intensities, but above the noise level they are very similar and reproduce the simulated curve on average.

## 6 Summary

We have used laser diffraction as an detection method for direct quantitative determination of the amplitudes of the director field in nematic electroconvection. Instead of the evaluation of the complete diffraction pattern, it is sufficient to record the second order diffraction spot, which is mainly influenced by the phase grating generated by the director field. An analytic treatment of the ray propagation in the LC layer by Fermat's principle provides the qualitative relation  $I_2/I_0 = \text{const.} \times \varphi_t^4$  at the second order diffraction reflex for small pattern amplitudes.

The proportionality constant can be derived from the material parameters using an analytical approach that considers at least the first non-linear term in light deflection in the calculation of the optical path of individual

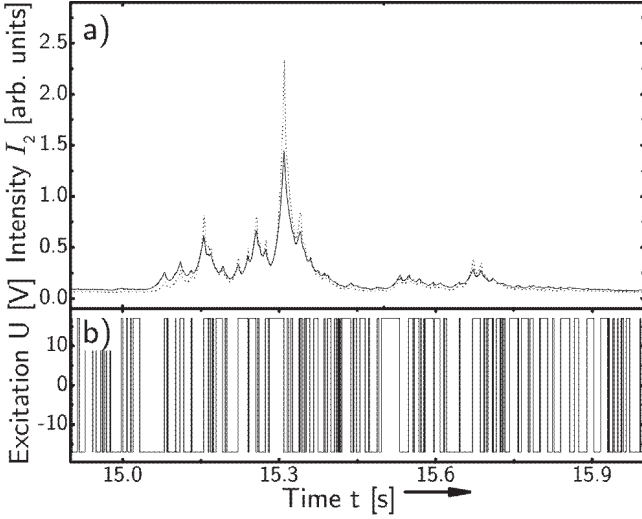


**Fig. 11.** Real time detection of director amplitudes in stochastically driven EHC, compared with a numerically simulated trajectory with the same realization of the driving process. The upper part (a) shows a measured intensity detected with the photodiode at the second order diffraction reflex (solid line), and a simulated curve (dotted line), both corresponding to the driving sequence depicted in (b).

light rays passing the cell. A numerical calculation of light propagation, which does not use mathematical approximations, except for the concept of ray optics, confirms the analytical result up to sufficiently large director deflections. The complete diffraction intensity profile calculated numerically is in good agreement with the profile measured experimentally. It has been shown that it is sufficient to use the simple relation Eq. (37) to determine the absolute value of the director deflection amplitude from the diffraction efficiency. We note, however, that a rigorous treatment of the problem of light propagation (for example by means of the FDTD method [44]) is the only exact treatment of the optical problem. It has not been achieved yet.

The derived quantitative relations have been used in three applications. In case of periodic sine wave excitation, the reported technique permits us to confirm the square root characteristics of the pattern amplitude in the pitchfork bifurcation of the stripe pattern. The non perfect behaviour at subcritical values is attributed to thermal fluctuations and a slight sample pretilt.

The agreement between analytically calculated growth and decay rates of the amplitudes of the director field and the measured light intensity at the second order reflex of diffracted light shows that one has to be very cautious when growth/decay rates are determined from laser diffraction intensities. The decay of the optical signal goes with the 4th power of the director deflections, and consequently, time constants differ by a factor of four.

The real-time quasi optical FOURIER transformation of the pattern gives an easy access to fast changing mode spectra or amplitudes, e.g. in case of stochastic driving. We have demonstrated the direct correlation between the

Parameter	cell 1 (2)	Exper. value
$n_o$	1.4935	1.4935
$n_e$	1.6315	1.6315
$\varepsilon_{\parallel}$	6.24	6.24
$\varepsilon_{\perp}$	6.67	6.67
$\sigma_{\parallel}$ [ $s^{-1}$ ]	90.0 (1350)	117.0
$\sigma_{\perp}$ [ $s^{-1}$ ]	60.0 (900)	90.0
$\alpha_1$ [ $g\ cm^{-1}s^{-1}$ ]	0.1	
$\gamma_1$ [ $g\ cm^{-1}s^{-1}$ ]	3.3	3.6
$\gamma_2$ [ $g\ cm^{-1}s^{-1}$ ]	-3.3	
$\beta$ [ $g\ cm^{-1}s^{-1}$ ]		
$\eta_1$ [ $g\ cm^{-1}s^{-1}$ ]	3.62	
$\eta_2$ [ $g\ cm^{-1}s^{-1}$ ]	1.0	
$K_{11}$ [ $g\ cm\ s^{-2}$ ]	$14.9 \times 10^{-7}$	$14.9 \times 10^{-7}$
$K_{33}$ [ $g\ cm\ s^{-2}$ ]	$13.76 \times 10^{-7}$	$13.76 \times 10^{-7}$

**Table 1.** Material parameters in Eq. (3) used in the calculations. Experimentally data for *Mischung 5* (last column) have been taken from [14, 45], measured conductivities correspond to the non-doped material. The unknown parameters and conductivities of the individual cells are obtained by fitting the corresponding threshold voltages and wave number characteristics for periodic ac driving to experimental data, see also Fig. 2.

driving electric field and the response of the director. Observation of the whole diffraction image instead of the trajectory of one representative diffraction peak may provide access to the development of the mode spectrum and access to dynamic mode selection in the stochastic driven system.

An important aspect in the experiment is the strong dependence of the diffraction image on small deviations from normal incidence. The problem of oblique incidence has been addressed first by Zenginoglou and Kosmopoulos [23]. In the appendix, we consider in detailed the dependence of the diffraction pattern from the angle of incidence of the laser beam. It is demonstrated that oblique incidence in general favors the reflexes of odd numbered order, which in first line reflect the amplitude grating produced by the director field.

The authors are particularly indebted to H. Schmiedel for helpful comments, discussions and critical reading of the manuscript. We acknowledge financial support from the Deutsche Forschungsgemeinschaft (Grant Be 1417/4 and SFB 294).

## References

1. A. Joets and R. Ribotta, Phys. Rev. Lett. **60**, 2164 (1988).
2. U. Bisang and G. Ahlers, Phys. Rev. Lett. **80**, 3061 (1998).
3. H. Riecke and G. D. Granzow, Phys. Rev. Lett. **81**, 333 (1998).
4. U. Bisang and G. Ahlers, Phys. Rev. E **60**, 3910 (1999).
5. P. Tóth, N. Éber, T. M. Bock, Á. Buka, and L. Kramer, Europhys. Lett. **57**, 824 (2002).
6. S. Rasenat, G. Hartung, B. L. Winkler, and I. Rehberg, Exp. Fluids **7**, 412 (1989).

7. S. Hirata and T. Tako, Jpn. J. Appl. Phys. **21**, 675 (1982).
8. K. Kondo, M. Arakawa, A. Fukuda, and E. Kuze, Jpn. J. Appl. Phys. **22**, 394 (1983).
9. J. A. Kosmopoulos and H. M. Zenginoglou, Appl. Opt. **26**, 1714 (1987).
10. A. Joets and R. J. Ribotta, J. de Physique **47**, 595 (1986).
11. A. Joets and R. J. Ribotta, Opt. Comm. **107**, 200 (1986).
12. H. Amm, M. Grigutsch, and R. Stannarius, Z. Naturforschung **53a**, 117 (1998).
13. H. Amm, M. Grigutsch, and R. Stannarius, Mol. Cryst. Liq. Cryst. **320**, 11 (1998).
14. H. Amm, R. Stannarius, and A. Rossberg, Physica D **126**, 171 (1999).
15. H. Amm, U. Behn, T. John, and R. Stannarius, Mol. Cryst. Liq. Cryst. **304**, 525 (1997).
16. T. Nagaya, T. Takeda, and H. Orihara, J. Phys. Soc. Jpn. **68**, 3848 (1999).
17. S. Akahoshi, K. Miyakawa, and A. Takase, Jpn. J. Appl. Phys. **15**, 1839 (1976).
18. L. K. Vistin' and S. S. Yakovenko, Soviet Physics **28**, 587 (1983).
19. H. Miike, Y. Kuriyama, H. Hashimoto, and Y. Ebina, J. Phys. Soc. Jpn. **53**, 3280 (1984).
20. T. O. Carroll, J. Appl. Phys. **43**, 767 (1972).
21. R. A. Kashnow and J. E. Bigelow, Appl. Opt. **12**, 2302 (1973).
22. M. Bouvier and T. Scharf, Opt. Eng. **39**, 2129 (2000).
23. H. M. Zenginoglou and J. A. Kosmopoulos, Appl. Opt. **27**, 3898 (1988).
24. H. M. Zenginoglou and J. A. Kosmopoulos, Appl. Opt. **28**, 3516 (1989).
25. H. M. Zenginoglou and J. A. Kosmopoulos, J. Opt. Soc. Am. A **14**, 669 (1997).
26. P. L. Papadopoulos, H. M. Zenginoglou, and J. A. Kosmopoulos, J. Appl. Phys. **86**, 3042 (1999).
27. H. M. Zenginoglou and P. L. Papadopoulos, J. Opt. Soc. Am. A **18**, 573 (2001).
28. T. John, U. Behn, and R. Stannarius, Phys. Rev. E **65**, 046229 (2002).
29. T. John, R. Stannarius, and U. Behn, Phys. Rev. Lett. **83**, 749 (1999).
30. U. Behn, T. John, and R. Stannarius, in *On-off intermittency and stochastically driven Convection in nematic liquid crystals*, edited by S. Boccaletti, B. J. Gluckman, J. Kurths, L. M. Pecora, and M. L. Spano (AIP Conf. Proc., American Institute of Physics, 2002), Vol. 622, p. 381.
31. L. Kramer and W. Pesch, Annu. Rev. Fluid Mech. **17**, 515 (1995).
32. L. Kramer and W. Pesch, in *Pattern formation in Liq. Cryst.* (Springer, NY, 1995).
33. S. Kai and W. Zimmermann, Progr. Theor. Phys. Suppl. **99**, 458 (1989).
34. W. Pesch and U. Behn, in *Evolution of Spontaneous Structures in Dissipative Continuous Systems*, edited by F. H. Busse and S. C. Müller (Springer, Heidelberg, 1998), p. 335.
35. H. Bohatsch and R. Stannarius, Phys. Rev. E **60**, 5591 (1999).
36. U. Behn, A. Lange, and T. John, Phys. Rev. E **58**, 2047 (1998).
37. S. Trainoff and D. Channell, Phys. Fluids **14**, 1340 (2002).
38. I. Rehberg, F. Horner, and G. Hartung, J. Stat. Phys. **64**, 1017 (1991).

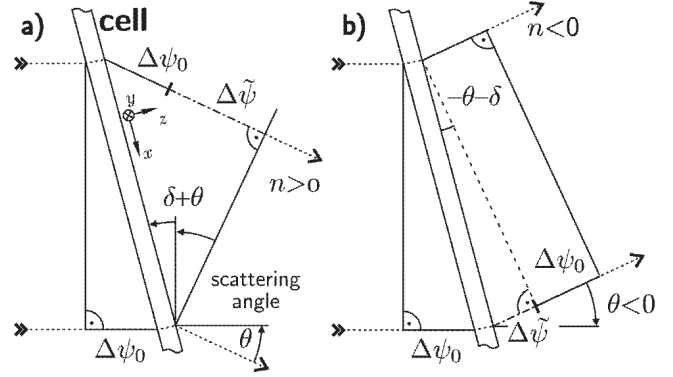


**Fig. 12.** A sketch of two light rays under oblique incidence separated by the wave length of the phase grating wave length  $\lambda_{ph}$ . The additional phase  $\Delta\psi'$  has to be considered in the calculation of the FRAUENHOFER diffraction for the positive (a) and negative (b) wings of the diffraction image.

39. H. Richter, S. Rasenat, and I. Rehberg, Mol. Cryst. Liq. Cryst. **222**, 219 (1992).
40. R. Lehner and G. Trigg, *Encyclopedia of Physics* (VHC Publishers Inc., New York, 1991).
41. I. Rehberg, S. Rasenat, M. de la Torre Juárez, W. Schöpf, F. Hörner, G. Ahlers, and H. R. Brand, Phys. Rev. Lett. **67**, 596 (1991).
42. M. A. Scherer, G. Ahlers, F. Hörner, and I. Rehberg, Phys. Rev. Lett. **85**, 3754 (2000).
43. M. A. Scherer and G. Ahlers, Phys. Rev. E **65**, 051101 (2002).
44. A. Taflove and S. C. Hagness, *Computational Electrodynamics: Finite-Difference-Time-Domain-Method* (Artech House, Boston, London, 2000).
45. M. Grigutsch and R. Stannarius, unpublished.

## A Diffraction at oblique incidence

The experiments show that the diffraction profile has a strong dependence on the tilt of the cell relative to the incident laser beam. A theoretical treatment with linearization has been published in [23]. In case of oblique incidence, where the cell is tilted in the  $(x, z)$  plane, the symmetry  $\theta \leftrightarrow -\theta$  is broken. The initial condition for Eq. (18) is now  $r'(z) = \tan \delta$ , where  $\delta$  is the entry angle of the laser beam into the LC-layer. We consider this in the numerical calculation of the beam propagation. In addition to this symmetry breaking, an extra phase  $\Delta\tilde{\psi}(\theta)$  appears. Figure 12 illustrates the origin of the additional phase difference. For the primary beam at  $\theta = 0$ ,  $\Delta\tilde{\psi}(\theta)$  vanishes. The symmetry breaking leads to a slight shift of the diffraction spots, and more obviously, to a change of the relative intensities of even and odd order spots. The condition allowing for the additional phase for constructive interference on the  $2n$ th even order spot ( $n > 0, \theta_n > 0$ ) is (see Fig. 12a)

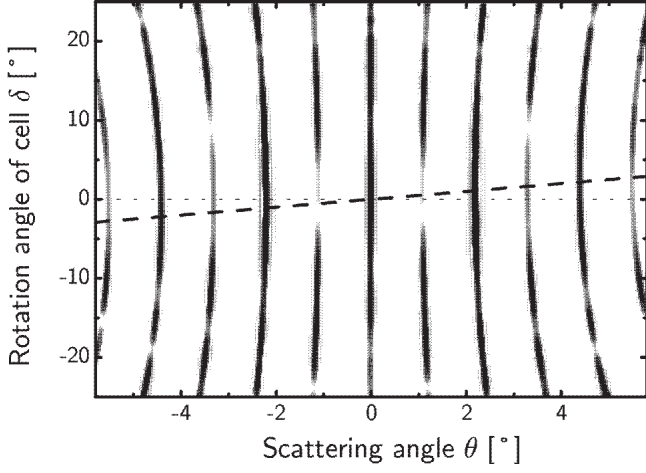


**Fig. 13.** Density plot from simulated diffraction profiles for oblique incidence and a  $\varphi = 0.4$  rad. The gray scale is logarithmic in the intensities. A cell thickness of  $25\text{ }\mu\text{m}$  and a pattern wave length of  $33\text{ }\mu\text{m}$  assumed. The dashed line marks  $\delta = \frac{1}{2}\theta$ .

$$\lambda_{\text{ph}} \sin(\theta_n + \delta) = \Delta\psi_0 + n \frac{2\pi}{k_L}, \quad (40)$$

$$\theta_n = \arcsin\left(\frac{2\pi n}{\lambda_{\text{ph}} k_L} + \sin \delta\right) - \delta; \quad n > 0 \quad (41)$$

and for  $\theta_n < 0$

$$\theta_n = \arcsin\left(\frac{2\pi |n|}{\lambda_{\text{ph}} k_L} - \sin \delta\right) + \delta; \quad n < 0, \quad (42)$$

where  $\lambda_{\text{ph}}$  is the wave length of the phase modulation of exiting light and  $k_L$  the wave number of the laser light. The diffraction intensity calculated numerically for a director modulation of  $\varphi = 0.4$  rad as a function of  $\theta$  and  $\delta$  is depicted in the density plot of Fig. 13. The most obvious result of the numerical calculation are the quantitative changes of the diffraction intensities with the cell rotation angle. Whereas the odd order maxima, which are mainly generated by the amplitude modulation, exhibit a minimum in the non-tilted cell and increased with a slight tilt of the cell, even order spots show qualitatively opposite behaviour. In the experiment we record the complete diffraction image on a diffusely scattering screen with a CCD camera (see Fig. 3) and scan the line  $y = 0$  (see Fig. 4a) from the digital image sequence. The camera gives only a qualitative picture of the intensities, not an exactly linear representation, but qualitative agreement with Fig. 13 is clearly acknowledged. We remark that the smallest diffraction angle  $\theta_n(\delta)$  for a given order  $n$  is not reached at  $\delta = 0$ , but

$$\frac{d}{d\delta}\theta_n = 0 \Rightarrow \sin \delta = \frac{1}{2} \frac{2\pi n}{\lambda_{\text{ph}} k_L} \approx \frac{1}{2} \sin \theta. \quad (43)$$

Its position is depicted as dashed line in Fig. 13 and coincides with the largest amplification/attenuation, resp., of the diffraction peak intensities.

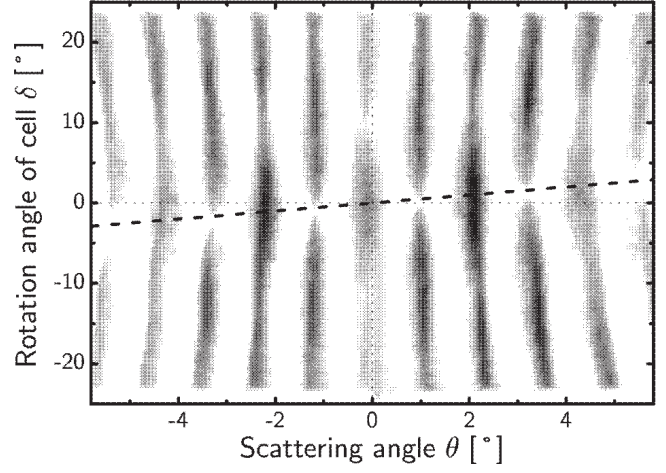


**Fig. 14.** Density plot of the measured diffraction profiles in inverse gray scale for a tilted cell. The profiles are taken in the midplane  $y = 0$  of the diffraction images of a stable convection pattern. The tilt of the cell to the incident beam leads to modulations of relative intensities and positions for all reflexes. One acknowledges the symmetry  $(-\delta, -\theta) \leftrightarrow (\delta, \theta)$ . The dashed line marks  $\delta = \frac{1}{2}\theta$  as in Fig. 13.